Electronic and optical properties of Si ⁄ Si O 2 nanostructures. I. Electron-hole collective processes in single Si ⁄ Si O 2 quantum wells

N. Pauc, V. Calvo, J. Eymery, F. Fournel, N. Magnea

To cite this version:

N. Pauc, V. Calvo, J. Eymery, F. Fournel, N. Magnea. Electronic and optical properties of Si ⁄ Si O 2 nanostructures. I. Electron-hole collective processes in single Si ⁄ Si O 2 quantum wells. Physical Review B: Condensed Matter and Materials Physics (1998-2015), 2005, 72 (20), ⟨10.1103/PhysRevB.72.205324⟩. ⟨hal-02060353⟩

PHYSICAL REVIEW B **72**, 205324 (2005)

Electronic and optical properties of Si/SiO_2 nanostructures. I. Electron-hole collective processes in single Si/SiO_2 quantum wells

N. Pauc,[1,*] V. Calvo,[1,†] J. Eymery,[1] F. Fournel,[2] and N. Magnea[1]
[1]*CEA Grenoble, DRFMC/SP2M/SiNaPS, 17 rue des Martyrs, 38054 Grenoble Cedex 9, France*
[2]*CEA-DRT-LETI, CEA/GRE, 17 rue des Martyrs, 38054 Grenoble Cedex 9, France*

(Received 3 June 2005; published 18 November 2005)

Photoluminescence measurements have been performed at low temperature on crystalline Si/SiO_2 quantum wells as a function of thickness. Three distinct electron-hole (e-h) phases are clearly identified in these structures: the electron-hole liquid, the electron-hole plasma, and the free-exciton gas. It is shown that spatial confinement induced by the SiO_2 barriers modifies the thermodynamical equilibrium between these phases with respect to the bulk case by changing the steady state of the carrier system and involving new transient states. In the low-thickness domain, the e-h recombination line blueshifts as a result of the effect of quantum confinement on the band-edge positions. Data are analyzed thanks to a model taking account of the new band-diagram parameters—effective mass, band degeneracy, anisotropy—and image charges in the dielectric barrier which modify the strength of Coulomb interactions between carriers in the Si well. Results interpreted in the frame of a simple coalescence model indicate that the two-dimensional electron-hole liquid forms a cloud of in-plane pancakes. Finally, an attempt is made here to compute the phase diagram of carriers in varying-thickness quantum wells by means of a spin-1 lattice-gas model and to predict the nature of the two-dimensional e-h collective state.

DOI: 10.1103/PhysRevB.72.205324 PACS number(s): 73.21.Fg, 78.55.−m, 78.67.De, 05.30.Fk

I. INTRODUCTION

In 1966 Haynes[1] observed a broad line in the photoluminescence (PL) spectra of bulk Si submitted to strong optical pumping. This new line, arising on the low-energy side of the free-exciton (FE) peak, was first attributed by the author to the radiative recombination of carriers in the excitonic molecule—namely, an entity composed of two electrons and two holes. In 1968, Keldysh[2] analyzed the results of Asnin and Rogachev[3] who observed a sudden jump in the conductivity of bulk Ge samples under variable-power illumination as the metallization of excitons. These results lead to a reinterpretation of Haynes' data and to attribute the broad low-energy line to a new electron-hole (e-h) phase, the electron-hole liquid (EHL). This condensed phase is obtained when excitons overlap and cannot form a bound state—that is, for sufficiently high excitonic densities. The band structure of Si is particularly suitable for the formation of EHL in view of the long exciton lifetime (of the order of 1 μs) resulting from the indirect nature of the band gap and from the orbital degeneracy of valence and conduction bands which lowers the positive kinetic part of the free energy per e-h pair.

Condensation of excitons in EHL was widely studied in bulk semiconductors during the 1960s and 1970s. It was therefore possible to compare the results of the many-body calculations to experimental measurements by considering several parameters such as EHL equilibrium density, kinetic, exchange, and correlation energies, etc. An excellent overview of the work accomplished in the field of EHL can be found in the review article by Rice *et al.*[4]

The overwhelming rise of the microelectronics industry during the past two decades has involved a significant improvement in nanofabrication techniques, particularly in the realization of silicon-based nanostructures with a very good crystallinity and a moderate concentration of nonradiative recombination centers at the Si/SiO_2 interface. It is nowadays possible to make artificial Si/SiO_2 heterostructures—namely, silicon-on-insulator (SOI) wafers, where a SiO_2/Si stack lies on a bulk-crystalline Si substrate after a molecular bonding stage.[5,6] The standard values for the SiO_2 and Si layers are set to 400 and 200 nm, respectively. A final thermal oxidation stage of the superficial crystalline Si (*c*-Si) layer is necessary to create a second barrier for the motion of carriers in the Si quantum well (QW) and to passivate the superficial defects. The resulting structure can be considered as a *c*-Si QW with quasi-infinite-height dielectric barriers of 3.2 eV for the electrons and 5 eV for the holes.

In 1998, Tajima and Ibuka[7] showed by continuous wave (cw) PL experiments that EHL could form in such structures. This discovery opened new opportunities for the study of EHL in low-dimensional Si samples.[8,9] Indeed, the QW thickness l_z can easily be tuned from the 200-nm standard value down to a thinner one by several thermal oxidation and HF etching deoxidation cycles. The excellent insulating, structural, and growth properties of the Si oxide give us a unique opportunity for the study of the various e-h phases and the Coulomb interactions between carriers in these Si QW's. In particular, interesting phenomena related to quantum confinement and mismatch of the dielectric constants in the heterostructure are expected to occur in narrow quantum wells with thickness of the order of the bulk excitonic Bohr radius a_x ($a_x \approx 4.9$ nm in crystalline silicon).

In this article, we present PL studies of *c*-Si QW's with thickness varying between 190 and 4.7 nm. Several regimes are identified according to the thickness domain. For 190 nm $\geqslant l_z \geqslant 3a_x \approx 15$ nm and within the spatial confinement regime, a first change in the thermodynamics of the e-h phases with respect to bulk Si is evidenced in *c*-Si QW's. For

$a_x \approx 4$ nm $\leqslant l_z \leqslant 3a_x \approx 15$ nm, in the weak quantum confinement regime, the EHL line shifts moderately towards high energies as a result of the quantum confinement effect on the band-edge positions. An attempt is made to account for these experimental results. The effect of image charges is included in a model that takes account of the low QW thickness thanks to a varying-l_z screened Coulomb potential. The question of the nature of the condensed phase in such QW's will be examined: Do we create an incompressible liquid or a compressible gas? A simple coalescence model will be used here to describe the spatial distribution of the two-dimensional EHL.

II. SAMPLES AND EXPERIMENT

The *c*-Si QW's are obtained from 8 in. SOI wafers where the *c*-Si and thermal SiO_2 layers have been transferred on a bulk Si substrate via molecular bonding. The variable-thickness *c*-Si QW set with l_z ranging from 15 to 190 nm originates from a series of thermally oxidized SOI wafers. The well thickness is defined by the amount of consumed *c*-Si during one or several oxidation-sacrificial deoxidation cycles resulting in a 400-nm buried oxide/l_z-nm *c*-Si/10–40 nm superficial oxide stack. We made a set of Si/SiO_2 QW's in the 5 nm $\leqslant l_z \leqslant$ 15 nm thickness range. Several mm^2-sized homogeneous samples can be obtained due to slow thickness variations with the lateral position. For each sample, we checked the thicknesses of the stack by means of spectroscopic ellipsometry. The accuracy of these measurements, confirmed by x-ray reflectivity, has been found to be lower than ±0.5 nm.

Samples were placed in a variable-temperature helium circulation cryostat with temperature T varying between 4 and 300 K. For cw PL experiments, we used a standard lock-in technique—i.e., a mechanically chopped Ar$^+$ cw laser, a 640-mm monochromator, and a photomultiplier tube with cooled InGaAs photocathode. The laser power reaches 100 mW under cw operation with a spot diameter $D_{nf} \approx 1250$ μm and $D_f \approx 55$ μm in the nonfocused and focused modes, respectively. The corresponding laser density powers $\mathcal{P}$ are found to be in the W cm^{-2} and kW cm^{-2} ranges. We recorded a white lamp spectrum (blackbody at 3400 K) and used it as a correction function of the spectra. We worked with the 351-nm (3.53-eV) laser line which provides strong absorption in the direct gap of *c*-Si and thus efficient pumping of silicon nanostructures. The absorbed part A of incident power by the *c*-Si QW's is assumed to obey the law $A(l_z) = (1-R)(1-\exp[-\alpha l_z])$ for a given l_z, where $\alpha = 9 \times 10^{15}$ cm^{-1} at $\lambda = 351$ nm is the inverse of the penetration length of laser beam in *c*-Si (Ref. 10) and R the reflected part. For time-resolved spectroscopy, we used a tripled Nd:YAG pulsed laser with 350 nm emission (duration pulse of 10 ns and variable repetition rate) and photon counting method to recover the signal.

III. SPATIAL CONFINEMENT REGIME

A. Effects at the thermodynamical steady-state equilibrium

The first step towards a best understanding of exciton condensation in confined media lies in identifying the distinct e-h phases generated in thick *c*-Si QW's and comparing them to the well-known EHL, EHP, and FE phases in bulk material. As shown in Fig. 1, one can see PL spectra obtained from a 100-nm QW for $T=6$, 15, and 35 K and various $\mathcal{P}$. For $T=6$ K and $\mathcal{P} = 4 \times 10^3$ W cm^{-2} the broad and asymmetric quasidegenerate TO-LO phonon replica of EHL in bulk Si arise in the PL spectrum at 1.081 eV. No energetic shift of the recombination lines is observed between 6.5 and 4×10^3 W cm^{-2} as a result of the constant density of the liquid in the QW under variable density of injected carriers. The slight redshift of the EHL line when $\mathcal{P}$ passes from 0.5 to 6.5 W cm^{-2} is attributed to the coalescence of EHL droplets. This phenomenon has been described in a previous paper[8] and is not the topic of this article.

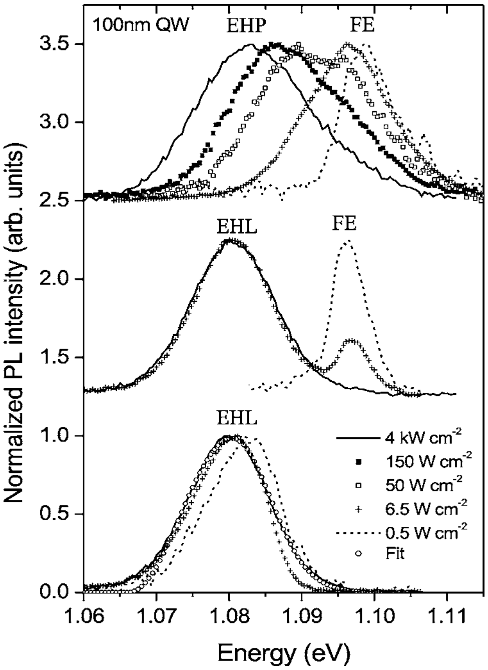

FIG. 1. Photoluminescence spectra obtained from a 100-nm *c*-Si QW at $T=6$, 15, and 35 K and $\mathcal{P}=0.5, 6.5, 50, 150$, and 4×10^3 W cm^{-2}.

A more accurate description of EHL ground-state parameters such as e-h pair density n or temperature can be given thanks to the line-shape analysis. EHL can be viewed as two degenerate incompressible gas of electrons and holes, each one with its own Fermi quasilevel E_F^e and E_F^h. Coulomb interactions between carriers lead to a band-gap renormalization—i.e., a decrease in the band-gap energy E_g by an amount ΔE_{BGR}, due to many-body phenomena. Following Rice,[11] we assume a rigid band shift without mass renormalization for electrons ($m_e = 1.08$) and holes ($m_h = 0.55$). The PL line shape is given by the product of convolution of the e-h populations and is written

$$I(h\nu) = I_0 \int_0^{h\bar{\nu}} \mathcal{D}_e(\epsilon)\mathcal{D}_h(h\bar{\nu}-\epsilon) \times f(\epsilon, E_F^e) f(h\bar{\nu}-\epsilon, E_F^h) d\epsilon, \tag{1}$$

where the prefactor I_0 is constant, $h\nu$ is the photon energy, $\mathcal{D}_{e,h}(\epsilon)$ are the tridimensional e-h density of states proportional to $\sqrt{\epsilon}$, f is the Fermi distribution, $h\bar{\nu}=h\nu-E_g-\Delta E_{BGR}+\hbar\omega_{TO}$ with $\hbar\omega_{TO}=58.3$ meV, the band-gap renormalization energy ΔE_{BGR} given in Ref. 12, and E_F^e and E_F^h given in Ref. 13.

The model line shape I is a function of three parameters I_0, n, and T, since $E_F^{e,h}$ and ΔE_{BGR} depend on (n,T) and n, respectively. A very convenient and accurate analytical form of the model function has been used here, where the continuous sum in Eq. (1) has been replaced by a discrete sum following the Gauss-Legendre integration method of order $j=12$.[14] Minimizing the χ^2 function with respect to (I_0,n,T) gives the experimental density n_{expt} and temperature T_{expt} for the EHL or EHP phases. Results from fits performed on the 100-nm QW spectrum for $T=6$ K and $\mathcal{P}=4$ kW cm^{-2} yield $n_{expt}=3.19\times10^{18}$ cm^{-3}, in very good agreement with theoretical calculations and experimental values of the equilibrium density of EHL in bulk silicon.[4] In Fig. 1, the fitted curve (circular symbol) is very close to the experimental data curve. We can conclude that at low temperatures EHL is stable in thick c-Si QW's and has the same ground-state parameters than in bulk samples. The fit temperature $T_{expt}=19$ K is found to be higher than the monitored temperature (6 K) for the highest pumping power—i.e., 4 kW cm^{-2}—whereas $T_{expt}=12$ K for moderate pumping powers—i.e., 6.5 W cm^{-2}. This discrepancy arises from local heating of the sample by a laser spot which is reinforced by inefficient heat transfer outside the well due to the thermal insulating properties of the silica barriers. Fortunately, T_{expt} is lower than the liquid-plasma transition temperature $T_c=28$ K in bulk c-Si. Therefore, the laser heating does not prevent e-h pair condensation in EHL in c-Si QW's.

In the spectra of Fig. 1 recorded at 15 K and for the low $\mathcal{P}$, one can see the two characteristic TO-LO phonon replica of FE resulting in a narrow line centered at 1.098 eV, as in bulk c-Si.[4] Due to many-body phenomena, EHL droplets can be viewed as potential traps for carriers with a barrier height or work function equal to $\Phi\approx8$ meV.[4] Thus evaporation of e-h pairs from EHL droplets to form excitons in QW's is thermally activated, as shown in Fig. 1 when T increases from 6 to 15 K for $\mathcal{P}=6.5$ W cm^{-2}. As $\mathcal{P}$ and the mean carrier density $\langle n\rangle$ increase, the EHL line intensity increases at the expense of the FE one. This change in the relative amplitudes of the recombination lines can be explained by the phase diagram of carriers in silicon:[4] an increase in $\langle n\rangle$ modifies the thermodynamical equilibrium between FE and EHL phases towards an increase in the ratio of "liquid" e-h pairs. The ability to modulate $\langle n\rangle$ by varying $\mathcal{P}$ in the SOI samples is due to the so-called "spatial confinement" effect caused by the dielectric barriers which prevents carriers diffusion in the c-Si substrate. In bulk c-Si, the high diffusion length of carriers, of the order of 100 μm,[4] induces a density gradient in the sample and a lowering of $\langle n\rangle$ with respect to c-Si QW's. In this case and in the frame of the theory of phase diagrams, no direct relation between $\mathcal{P}$ and $\langle n\rangle$ can be given to account for the relative amplitudes of the FE and EHL lines.

The spectra recorded for $T=35$ K show a clear blueshift of the e-h recombination line as $\mathcal{P}$ decreases. This shift is ascribed to a lowering of the absolute value of the renormalization energy ΔE_{BGR} resulting from a decrease in the e-h fluid density n.[12] This allows us to identify this fluid with the electron-hole plasma (EHP) which has been found to be the stable condensed e-h phase above $T\approx28$ K in bulk silicon.[15,16] As a consequence, we deduce that the liquid-plasma transition temperature T_c in the 190-nm c-Si QW is likely close to its bulk value—strictly speaking and according to the spectra acquired at $T=15$ and 35 K as shown in Fig. 1 for $\mathcal{P}=6.5$ W cm^{-2}, T_c is found be in the 15–35 K range, in qualitative agreement with the theoretical and experimental bulk values. In the case of very low pumping powers we can see two contributions in the PL spectra which correspond to the convergence of the EHP line towards the FE one. Finally, for the lowest $\mathcal{P}$, the only stable e-h system in the QW is the FE phase. The observed progressive change in the ratio of EHP and FE lines is an example of the Mott transition between the metallic EHP and the insulating FE phases which occurs not only in bulk c-Si[17] but also here in the c-Si QW's.

The spatial confinement effect is a very useful phenomenon which helps us in determining the different phase densities in the QW. Considering the high diffusion length of carriers with respect to the well thickness, one can assume a total filling of the QW in EHP or FE phases, for the very-high- and very-low-$\mathcal{P}$ regimes where no mixing between EHP and FE occurs. Measuring the lifetime $\tau^{p,e}$ of e-h pairs in EHP and FE phases for the 190-nm QW at 35 K allows us to calculate the plasma or excitonic pair densities $n^{p,e}$ as

$$n^{p,e}\approx\frac{\mathcal{P}\tau^{p,e}(1-R)}{l_z h\nu},\tag{2}$$

where $R\approx0.55$ is the reflection coefficient of laser beam on the SOI surface.

Assuming that the Mott transition for carriers in the 190-nm QW occurs between $\mathcal{P}=6.5$ and 0.5 W cm^{-2} and taking $\tau^p=800$ ns and $\tau^e=2700$ ns for the 190-nm QW at 35 K, Eq. (2) yields $n^p=2.7\times10^{17}$ cm^{-3} and $n^e=6.8\times10^{16}$ cm^{-3}—note that the excitonic contribution in the 6.5 W cm^{-2} spectrum in Fig. 1 has been neglected. Knowledge of the Debye-Huckel screening length $\lambda_{DH}=(2e^2n/\epsilon_0\epsilon_{Si}k_BT)^{-1/2}$, where $\epsilon_{Si}=11.4$ is the dielectric constant of c-Si, allows us to calculate the Mott density n_M with the condition[18] $\lambda_{DH}(n\geqslant n_M)\leqslant0.84a_x$ which gives

$$n_M(T)=\frac{1.19^2\epsilon_0\epsilon_{Si}k_BT}{2e^2a_x^2}.\tag{3}$$

Thanks to Eq. (3), for $T=35$ K, we find $n_M\approx5.3\times10^{16}$ cm^{-3}. This theoretical value is somewhat smaller than the measured experimental one in the 6.8×10^{16}–2.7×10^{17} cm^{-3} range. This discrepancy can be corrected by taking into account the lateral diffusion of carriers along the QW which induces a lowering of n as calculated with Eq. (2). When carriers are generated by a $D_{nf}=1250$ μm diameter laser spot with $\mathcal{P}=0.5$ W cm^{-2}, the exciton diffusion length $L_{EX}=\sqrt{D_{EX}\tau_{EX}}\approx630$ μm, with $D_{EX}=1500$ cm^2 s^{-1}[4], gives the characteristic radial spreading of the e-h system. The density given in Eq. (2) should be modified and divided by a density correction factor c to take account of the lateral diffusion of carriers. Here, the evaluation of c is straightfor-

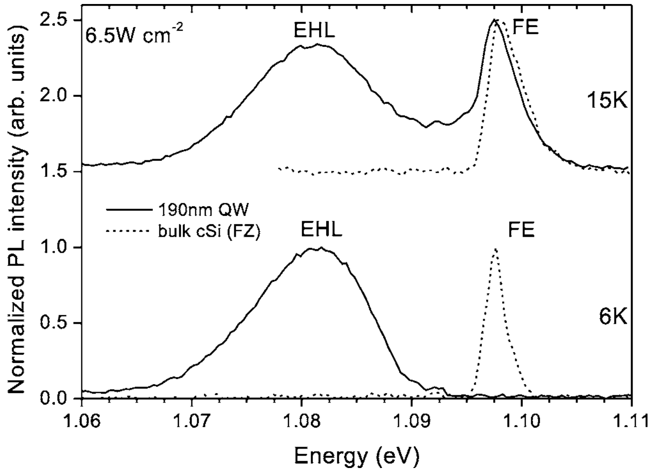

FIG. 2. Comparison between PL spectra from a 190 nm c-Si QW and pure bulk c-Si floating zone (FZ) under the same power density $\mathcal{P}=6.5$ W cm^{-2} for $T=6$ and 15 K.

ward and gives $c=[(D_{nf}/2+L_{EX})/D_{nf}/2]^2\approx 4$ and results in a more accurate estimate of the experimental density n_M in the 1.7×10^{16}–6.75×10^{16} cm^{-3} range, in good agreement with the theoretical values.

The former approach used to calculate n is simple and crude but the good estimate of n_M supports our hypothesis on the limited expansion of an EHP or a FE gas between the SiO$_2$ barriers—i.e., the spatial confinement effect.

Another striking effect relative to the spatial confinement phenomenon can be observed in Fig. 2 by comparing the PL spectra of a 190-nm c-Si QW and a bulk c-Si under the same conditions of illumination and temperature. For either $T=6$ or 15 K and $\mathcal{P}=6.5$ W cm^{-2}, we can see that the PL spectra of the bulk sample only exhibit the FE line, whereas those of the QW contain the two EHL and FE contributions. We conclude that the exciton condensation threshold as a function of $\mathcal{P}$ is lowered in the Si-confined systems such as SOI QW's, due to the limited two dimensional diffusion of carriers.

We would like to point out that the photoconduction experiment of Asnin and Rogachev[3] performed in bulk germanium could be particularly interesting when applied in our samples. Indeed, spatial confinement along with the ability to control the geometry of the Ohmic contacts at the QW surface allow not only accurate measurement of the carrier density but also measurement of the fluid resistivity between the two electrodes. Measuring the position of the conductivity jump by increasing the laser power would give an accurate estimate of the Mott density. In addition, in case of total filling of the QW volume by the EHL at high $\mathcal{P}$, measurement of the EHL resistivity is expected to give precious information on its metallic nature and on the "hydrodynamical" properties of this condensed phase.

B. Dynamical effects

Under cw operation, the EHL, EHP, and FE phases are in a thermodynamical steady-state equilibrium since the thermalization time of carriers (of the order of 1×10^{-12} s) is several orders of magnitude smaller than the e-h lifetime (of the order of 1×10^{-6} s). Due to the long integration time of the PL signal by our lock-in amplifier in the cw PL detection display (of the order of 1×10^{-3} s), no dynamical effects can be observed. To overcome this problem, we performed time-resolved PL measurements with a pulsed laser and a digital counter. Two adjustable time parameters are used: the time delay (D) after the end of the laser pulse to open the counting window and the width (W) of the counting window.

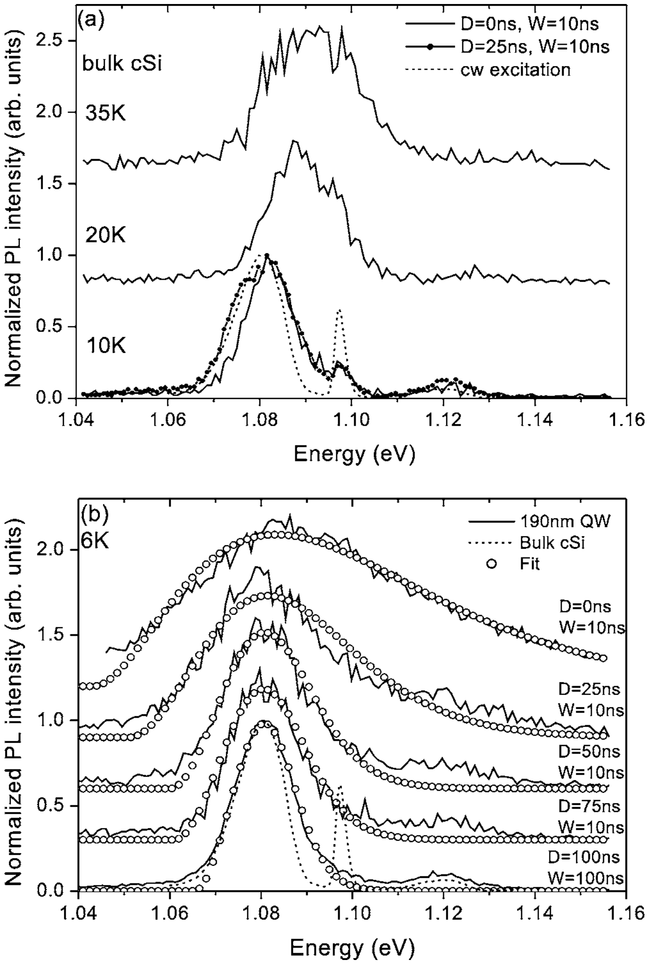

FIG. 3. (a) Solid and circle lines: time-resolved PL spectra obtained on bulk c-Si for a delay after pulse $D=0$ ns and a width of the counting window $W=10$ ns as a function of temperature and $D=25$ ns and $W=10$ ns at $T=10$ K respectively. (b) Solid lines and circles: time-resolved PL spectra obtained on a 190-nm c-Si QW as a function of D and W and fits, respectively. Dotted line: PL spectrum of c-Si under cw operation at $T=10$ K for (a) and (b).

Time-resolved PL spectra have been recorded on bulk c-Si and the 190-nm c-Si QW samples, as shown in Figs. 3(a) and 3(b) for various temperatures, delays, and widths. D and W are set to small values to avoid the "time integration phenomenon" which would cause distortion of PL spectra towards a "classical" equilibrium line shape.

We can see in Fig. 3(a) that the spectrum recorded under pulsed operation for $D=0$ ns, $W=10$ ns, and $T=10$ K on the bulk c-Si is close to the TO-LO EHL replica observed under cw operation. The slight energetic shift between these two spectra might be due to e-h recombination in small EHL droplets in maturation at short delays. Such a blueshift has also been observed under cw operation in thin QW's at low temperatures and ascribed to carrier recombination via the fundamental states of a "nanodroplet," viewed as a three-dimensional (3D) harmonic oscillator for electrons and holes.[8] With increasing D—i.e., for $D=25$ ns and $W=10$ ns—the EHL line redshifts and has the same low-energy cutoff as the cw EHL line corresponding to macroscopic droplets. Thus, the maturation time necessary for embryos to reach a bigger equilibrium size in bulk c-Si is lower than 25 ns. The slight broadening observed on the high-energy side of the spectrum recorded for $D=25$ ns and $W=10$ ns compared to cw excitation is ascribed to sample heating caused by laser beam.

With increasing temperature, a clear blueshift of the recombination line occurs and proves that carriers undergo the phase transition between EHL and EHP, even at small D. The transition temperature is found to be between 10 and 20 K and remains lower than the theoretical estimate of 28 K. This numerical result should be reevaluated in view of the very high density power of the laser beam. Indeed, the electronic temperature is to be higher than the cryostat probe temperature since a crude estimate gives $\mathcal{P}\approx 30$ MW cm^{-2}, which is several orders of magnitude higher than the power densities used in cw experiments.

Spectra recorded for the 190-nm QW under the same conditions than bulk material are reported in Fig. 3(b) and show a clear broadening at short delays. With increasing time ($D\approx 100$ ns), the recombination spectra tend to the well-known TO-LO EHL replica at 6 K. We performed fits on the data as we did in the cw regime by using Eq. (1), 3D e-h density of states and the gap renormalization energy given in Ref. 12. We used the generalized expression of Balslev[19] for the quasi-Fermi levels of electrons and holes which is valid both in the classical and quantum limits and adds to ΔE_{BGR} the thermal energetic deviation of the band gap. Following Ref. 20, this negative contribution reads $AT+CT^2$, with $A=1.059\times 10^{-5}$ eV K^{-1} and $B=-6.05\times 10^{-7}$ eV K^{-2}. Experimental results for n and T are reported in Fig. 4(a) and show a decrease of the density and temperature with time. For $D=0$ ns, the density is found to be smaller than its expected value in view of the general shape of the $n(D)$ curve. This discrepancy might be due to a partial occupation of the split-off band by holes resulting in a change in the 3D density of states. Indeed, for $n\approx 10\times 10^{18}$ cm^{-3} and $T\approx 200$ K, an estimate of the hole Fermi quasilevel E_F^h using Balslev formulas gives $E_F^h\approx 20$ meV, which is very close to the energy splitting of the valence band due to spin-orbit coupling (about 40 meV in c-Si). We conclude that a dense and hot e-h plasma is created just after the end of the laser pulse in the QW, unlike in the bulk c-Si sample. In such bulk samples, the ability of free carriers to expand in all the volume of the material moderates the plasma density, even at short delays, and involves the formation of a cold EHL. Comparison between data from the QW and the bulk sample clearly indicates that the rise in temperature is much greater in SOI than in bulk c-Si, which is not surprising considering the limited heat transfers in the quantum well due to the good thermal insulation properties of the SiO$_2$ barriers.

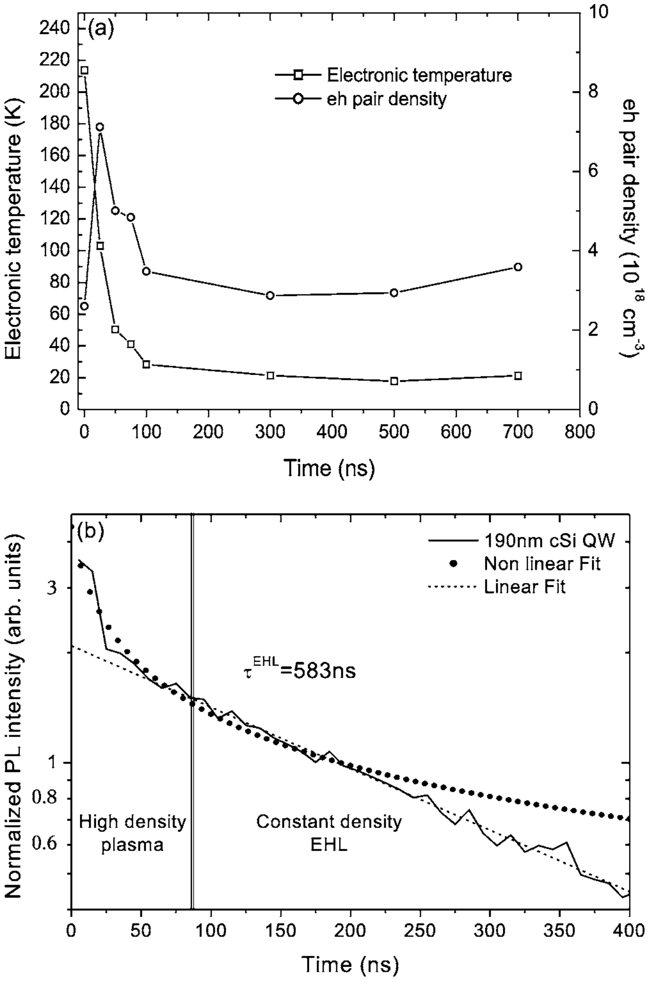

FIG. 4. (a) Squares and circles: experimental electronic temperature and pair density as a function of delay after laser pulse, as deduced from fits performed on spectra from Fig. 3(b). (b) Solid curve: decay curve at $\lambda=1.146$ μm of e-h radiative recombination for $T=6$ K in the 190-nm QW. Dotted curve: linear fit of the decay curve. Circles: nonlinear fit of the decay curve using the model function (5).

As we can see in Fig. 4(a), the metastable high-density e-h plasma rapidly relaxes towards a constant-density-cooled EHL with $n\approx 3\times 10^{18}$ cm^{-3}. A crude estimate of this relaxation time τ^r gives $\tau^r\approx 100$ ns. This shows unambiguously that the e-h system goes through a nonequilibrium transient state to the quasiequilibrium EHL state thanks to the spatial confinement effect in SOI QW's.

A supplementary proof of the observation of this transient state can be given by measuring the e-h lifetime at 1.146 μm (1.081 eV), as reported in Fig. 4(b) for $T=6$ K in the 190 nm QW. The logarithmic plot of the decay curve is divided into a "classical" linear part and a nonlinear part at short delays ($D\leqslant 100$ ns). Neglecting the nonlinear part of the curve corresponding to the high-density metastable plasma gives us the EHL lifetime $\tau^{EHL}=583$ ns, which is in good agreement with bulk results.[4] The recombination rate in c-Si is governed by nonradiative Auger processes so that the total EHL lifetime reduces to the Auger contribution τ^A. Assuming a strong carrier injection, we can set $\tau^{EHL}\approx(\gamma n^2)^{-1}$, where $\gamma=\gamma^e+\gamma^h$ is the sum of the e-e-h and h-h-e Auger processes and $n=2.9\times 10^{18}$ cm^{-3} is the experimental EHL density [see

Fig. 3(b)]. Comparing the measured and theoretical EHL lifetimes gives the experimental Auger coefficient $\gamma \approx 2.0 \times 10^{-31}$ cm^6 s^{-1}, in very good agreement with bulk values[4] giving 3×10^{-31} cm^6 s^{-1} at 2 K.

The kinetic equation for carrier recombination is written

$$\frac{d\langle n\rangle}{dt} = -\frac{1}{\tau^A}\langle n\rangle(t), \qquad (4)$$

where $\langle n\rangle$ is the carrier mean density and cannot exceed the EHL droplet carrier density, which corresponds to a local e-h condensed state. Keeping constant τ^A gives the well-known exponential decay function $\langle n(t)\rangle = \langle n_0\rangle \exp[-t/\tau^A]$ for the time-resolved PL spectrum of constant-density EHL droplets—note that in Eq. (4), τ^A only depends on the *local* carrier density n. At small delays, the intrinsic plasma density n has been found to vary rapidly, so that τ^A is no longer constant and involves a change in the shape of the decay curve. Assuming a 100% filling factor of the QW by the e-h plasma after the end of the intense laser pulse, we can set $\langle n\rangle = n$ and $\tau^A = (\gamma\langle n\rangle^2)^{-1}$. Integrating Eq. (4) with respect to $\langle n\rangle$ gives the relation

$$\langle n(t)\rangle = (2t\gamma + \langle n_0\rangle^{-2})^{-1/2}, \qquad (5)$$

where $\langle n_0\rangle$ is the initial carrier density.

Using the model function (5) and the experimental value of the Auger coefficient at large delays, we performed a fit on the nonlinear part of the decay curve in Fig. 4(b) (circles) and found $\langle n_0\rangle \approx 15 \times 10^{18}$ cm^{-3}, which is in good agreement with the expected value of the e-h pair density as deduced from line-shape fits [see Fig. 4(a)].

This result supports our hypothesis on the formation of a dense, metastable, and uniform plasma at short delays. With increasing time, the e-h system undergoes a relaxation towards a more dilute condensed state to form a cloud of cooled EHL droplets with constant intrinsic density n. The linear part of the decay curve reported in Fig. 4(b) is ascribed to a decrease of the droplet radius and/or a reduction of the droplet number with a constant intrinsic pair density.

IV. WEAK QUANTUM CONFINEMENT REGIME

A. Effect of the thickness lowering

In view of the ability to modulate the c-Si thickness l_z by adjusting the consumed silicon thickness during the oxidation/deoxidation cycles, cw PL experiments as a function of l_z become accessible in Si/SiO$_2$ QW's from $l_z = 190$ nm down to $l_z = 4.7$ nm, as reported in Fig. 5.

Spectra reported in this figure show unambiguously that the well-known asymmetrical EHL line centered at 1.081 eV in bulk or thick c-Si QW's progressively blueshifts when $l_z \leqslant 15$ nm $\approx 3a_x$, as a result of the quantum confinement effect on the carrier band-edge positions. The other lines centered at 1.098 and 1.091 eV originate from FE and bound-exciton (BE) on boron recombination, respectively, either in the QW if $l_z \geqslant 28$ nm or in the substrate if the QW turns to be transparent to the laser beam for $l_z \leqslant 13$ nm.

An important question arises from the changes in the band diagram of c-Si at low l_z: Do we create an incompressible quasi-two-dimensional EHL or a compressible quasi-two-dimensional EHP? Lowering the dimensionality of the semiconductor leads to a rise of the valence- and conduction-band degeneracy and to a modification of the carrier masses. This results in serious changes in the kinetic, exchange, and correlation terms of the e-h pair energy $F(r_s)$ and can be an obstacle for the realization of the minimum-energy condition of $F(r_s)$ necessary for the e-h system to reach its liquid equilibrium state. This problem was briefly described in a previous Letter,[8] but no detailed method or model was presented. Obviously, results of future calculations must show that the 2D EHL or 2D EHP binding energy is greater than the corresponding exciton binding energy to account for the observation of the condensed phase luminescence. On the contrary, a larger exciton binding energy would involve the destruction of the condensed phase to the benefit of the excitonic phase and would lead to a narrow PL line.

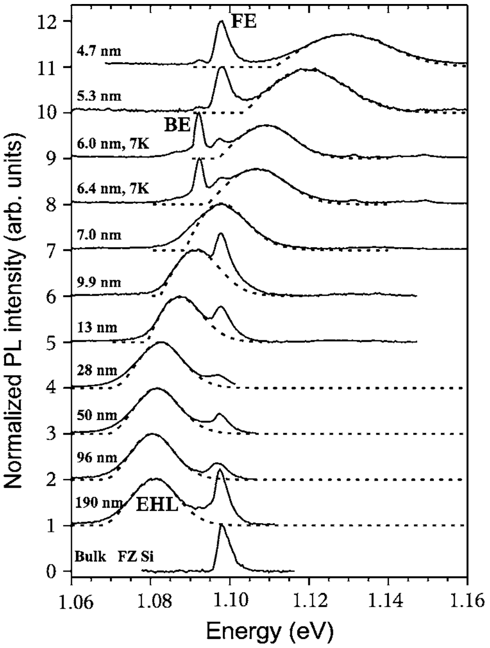

FIG. 5. Solid curves: continuous-wave PL specta acquired on variable-thickness c-Si QW's for $\mathcal{P} = 6.5$ Wcm^{-2} and $T = 15$ or 7 K. Dotted curves: 3D ($l_z \geqslant 28$ nm) and 2D ($l_z \leqslant 13$ nm) fits performed on data using the model functions (1) and (13), respectively.

Here, we shall adapt the model of Kleinman[21] to the case of silicon. Assuming a size reduction of the QW in the (100) direction and following Ando and Stern,[22] we get $g = 2$ for the number of populated electron valleys with the greater mass for motion perpendicular to the QW surface. The 2D density-of-states mass is written $m_e = m_{et}$, where $m_{et} = 0.19$ (Ref. 4) is the bulk transversal electron mass. The hole-band degeneracy is raised to 1 with $m_h^{-1} = \frac{1}{2}(2m_{hH})^{-1} + \frac{3}{2}(2m_{hL})^{-1} \approx (0.19)^{-1}$,[23] the inverse of the 2D density-of-states mass of holes, $m_{hH} = 0.523$ and $m_{hL} = 0.154$ (Ref. 4) the heavy- and light-hole masses in the bulk material, respectively.

In the frame of the Kleinman's theory, the screened Coulomb potential $v(r_s^{2D})$ varies with l_z through a thickness-dependent screening parameter $\gamma(l_z)$ and we have

$$v(r_s^{2D}) = \pm 2\frac{1-\exp[-\gamma(l_z)r_s^{2D}]}{r_s^{2D}}, \tag{6}$$

where v and r_s^{2D} are expressed in 2D Rydberg and Bohr radius units, respectively. When applied to our QW, these units read $a_x^{2D}=(4\pi\epsilon_0\epsilon_{Si}\hbar^2/e^2)[m_h^{-1}+m_e^{-1}]\approx 6.4$ nm and $Ry^{2D}=e^2/8\pi\epsilon_0\epsilon_{Si}a_x^{2D}\approx 9.9$ meV.

For silicon, the γ function is deduced from the scale relation

$$l_z^{Si} = \frac{a_x^{2D}(Si)}{a_x^{2D}(GaAs)} l_z^{GaAs}(\gamma), \tag{7}$$

thanks to the established $\gamma(l_z)$ function given for GaAs in Table I of Ref. 21.

A more accurate description of the many-body phenomena in the QW's must include the effect of image charges on the strength of the e-h interactions due to the great dielectric mismatch between Si and SiO$_2$. The potential energy v_{im} resulting from the interaction between a carrier and its image charge, both symmetrically localized with respect to the Si/SiO$_2$ interface, is written

$$|v_{im}(z)| = \frac{1}{4\pi\epsilon_0\epsilon_{Si}}\frac{\epsilon_{Si}-\epsilon_{SiO_2}}{\epsilon_{Si}+\epsilon_{SiO_2}}\frac{e^2}{2z}, \tag{8}$$

in SI units, with $\epsilon_{Si}=11.4>\epsilon_{SiO_2}=3.9$. As an example, taking a carrier in the middle of a 5-nm QW allows us to give the order of magnitude of the "image" contribution $|v_{im}|\approx 12$ meV with respect to the nonperturbed "Kleinman" potential $v(r_s^{3D}\approx 0.86)\approx 29.9$ meV ($r_s^{3D}\approx 0.86$ corresponding to the 3D liquid equilibrium density). In view of these values, SOI QW's appear as unique samples in which effects of image charges are expected to play an important role on the electronic and optical properties.

In order to take account of the influence of image charges in the potential of QW carriers, we use the theory of Keldysh[24,25] which gives the l_z dependence of the exciton binding energy $B_{EX}(l_z)$ in planar semiconductor-dielectric nanostructures:

$$B_{EX}(l_z) = \frac{e^2}{4\pi\epsilon_0\epsilon_{Si}l_z}\left[\ln\left(\frac{\epsilon_{Si}^2}{\epsilon_{SiO_2}^2}\frac{l_z}{a_x^{3D}}\right) - C\right]$$

$$\text{for } \frac{\epsilon_{SiO_2}^2}{\epsilon_{Si}^2}a_x^{3D} < l_z < a_x^{3D}, \tag{9}$$

$$B_{EX}(l_z) = \frac{e^2}{4\pi\epsilon_0\epsilon_{Si}l_z}\left[\ln\left(\frac{\epsilon_{Si}^2}{\epsilon_{SiO_2}^2}\sqrt{\left(\frac{l_z}{a_x^{3D}}\right)^2 + 4\pi^2\frac{E_x^{3D}}{E_g}}\right) - C\right]$$

$$\text{for } l_z < \frac{\epsilon_{SiO_2}^2}{\epsilon_{Si}^2}a_x^{3D}, \tag{10}$$

where $C\approx 0.577$ is the Euler constant, E_x^{3D} the bulk exciton binding energy, and $E_g=1.170$ eV the bulk band gap at $T=6$ K.

The new screening parameter modified by the image charges is obtained by solving the two-equation system arising from the variational principle starting from the γ-dependant model potential (6) and from a test exciton wave function[23]

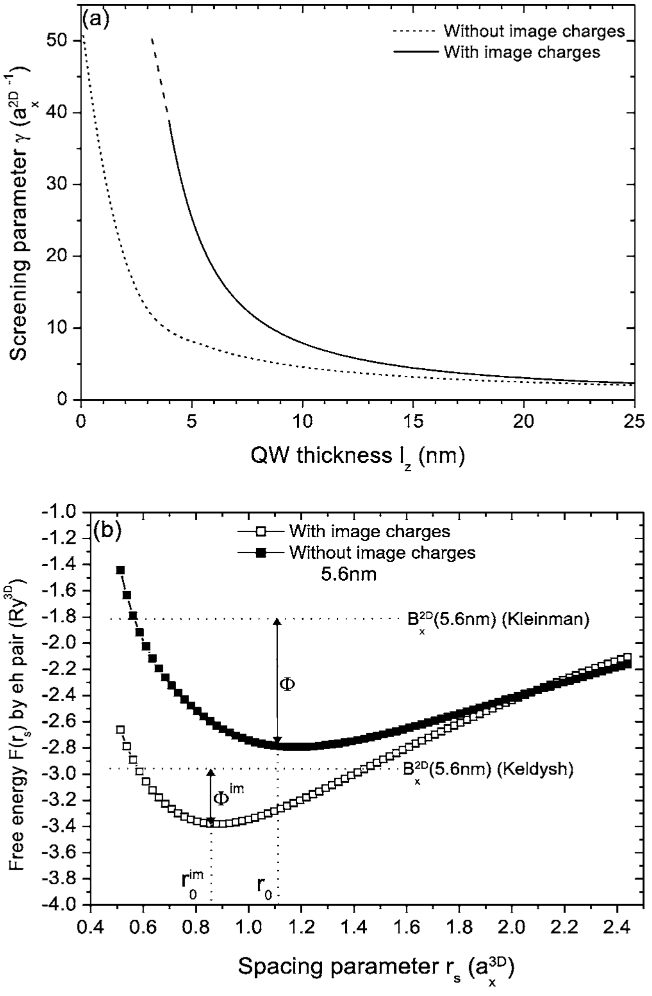

FIG. 6. (a) Screening parameter γ as a function of the QW thickness with or without the image charges effect (solid and dotted curves, respectively). (b) Free energy as a function of r_s for the 5.6-nm QW with or without the image charges effect (open and solid squares, respectively).

$$\gamma = p^3/[2(1+p/2)^2], \tag{11}$$

$$B_{EX} = [2\gamma/(1+p/2)] - \gamma^2/p^2, \tag{12}$$

when B_{EX} takes its "image" value for a given l_z as given in Eqs. (9) and (10).

The free energy by e-h pair at zero temperature is computed numerically and is the sum of the average kinetic energy of a totally degenerate e-h plasma $E_F=(E_F^e+E_F^h)/2$ and of the exchange and correlation terms E_X and E_C, as described in Ref. 21.

As shown in Fig. 6(a), $\gamma(l_z)$ decreases with l_z, with or without including the image charges effect.[26] Keeping in mind Eq. (6), we deduce that the lowering of the dimensionality involves an increase in the Coulomb energy per e-h pair at fixed r_s^{2D}, which is reinforced by the image charge introduction.

The complete calculation of the free energy per e-h pair reported in Fig. 6(b) shows that F has a local minimum at the (r_0, E_G) point, where $|E_G|$ denotes the liquid binding energy, and that $|E_G - B_{EX}| = \Phi > 0$ (Φ being the exciton work function). This qualitatively justifies the observed spectra in Fig. 5 as originating from a condensed e-h phase and *a priori* predicts a liquid formation. Moreover, Fig. 6(b) clearly shows that image charges are responsible from an increase in $|E_G|$ and in the equilibrium density $n_0^{2D} = (\pi r_0^{2D} a_x^{2D})$. This result goes in the same way as the strengthening of the Coulomb interaction observed in Fig. 6(a) and proves that image charges contribute to the liquid stabilization.

Systematic calculations of the free-energy functions have been performed for various l_z in the 4–22 nm range with or without the image charge effect. They indicate an increase of $|E_G|$ and Φ with decreasing l_z, in agreement with Kleinman's results for (100) Ge QW's,[21] and larger numerical values when introducing the image charges, which confirms their stabilizing properties upon the liquid.

No excitonic contribution appears on PL spectra in Fig. 5. This experimental observation could be ascribed to a significant increase in the exciton work function which would modify the liquid-gas equilibrium and would favor liquid formation at the expense of the exciton gas. As mentioned above, calculations corroborate experiments and tend to show that the 2D liquid binding energy increases more rapidly than the exciton binding energy as l_z is lowered.

Data in Fig. 5 were analyzed with the 3D model function (1) for $l_z \geqslant 28$ nm and with the 2D model function

$$L(h\nu) = L_0 \int_0^{h\bar{\nu}} f(\epsilon, E_F^e) f(h\bar{\nu} - \epsilon, E_F^h) d\epsilon \tag{13}$$

for $l_z \leqslant 13$ nm. In Eq. (13), L_0 is constant and E_F^e and E_F^h are the 2D e-h Fermi levels given in Ref. 21. The new spectroscopic band gap $E_g' = h\nu - h\bar{\nu}$ must include the effects of the quantum confinement energy on the band-edge positions and the changes in the band-gap renormalization energy induced by the modification of the exchange-correlation energy $F_{xc}(r_s^{2D})$ in the low-dimensional e-h system. Several works concerning calculations of the quantum confinement energies in c-Si nanostructures are reported in the literature.[27,28] Here, we shall use the *ab initio* calculations of Niquet *et al.*[29] which give the quantum confinement energy in (100) c-Si QW's as a function of l_z. The fits of these calculated values give for the valence- and conduction-band edge positions

$$E_v(l_z) = \frac{K_v}{l_z^2 + a_v l_z + b_v}, \tag{14}$$

$$E_c(l_z) = \frac{K_c}{l_z^2 + a_c l_z + b_c} + E_g, \tag{15}$$

where l_z is in nm, $K_v = -1326.2$ meV nm^2, $a_v = 1.418$ nm, $b_v = 0.296$ nm^2, $K_c = 394.5$ meV nm^2, $a_c = 0.939$ nm, and $b_c = 0.324$ nm^2. For a given thickness, ΔE_{BGR} is computed numerically from the F_{xc} function following Eq. (34) in Ref. 21. Finally, for fitting, the r_s^{2D}-dependent spectroscopic gap, introduced in Eq. (13) is written

$$E_g' = E_c - E_v + \Delta E_{BGR} - \hbar\omega_{TO}. \tag{16}$$

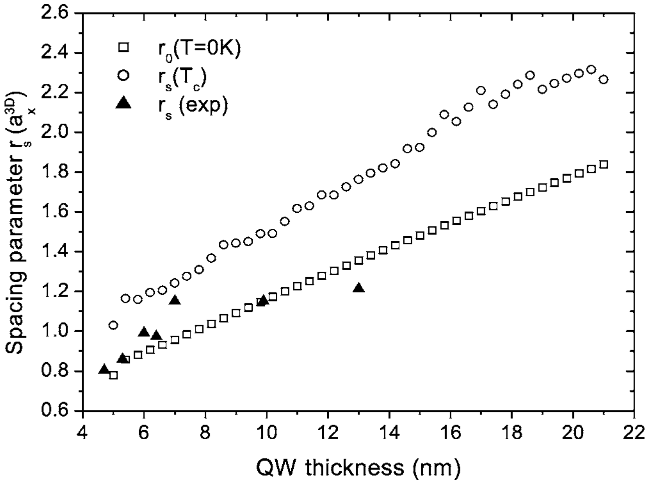

FIG. 7. Experimental densities of the 2D e-h system (triangles), as deduced from fits performed on spectra in Fig. 5, calculated interparticle spacing parameters at zero temperature (squares), and T_c (circles).

Results of 2D fits are reported in Fig. 7 in bulk units. For more convenience in interpreting the results, we have calculated the critical interparticle spacing parameter at the liquid-plasma transition temperature T_c in the explored l_z domain. A crude estimate of T_c can be made by examining the temperature-dependent energy function E per e-h pair. In complete analogy with the 3D case,[15] we can set $E(n^{2D}, T)$ as the sum of the free energy at zero temperature and of a T term linked to the 2D plasma specific heat, and we have

$$E(n^{2D}, T) = F(n^{2D}) - \frac{\pi}{6 n^{2D} \hbar^2} (k_B T)^2 (m_h + g m_e) \tag{17}$$

in SI units. The critical temperature is reached when $E(n^{2D}, T)$ has no more local minimum.[30]

Experimental densities are found to be within the "liquid" domain located between the squares and circles (cf. Fig. 7), when image charges are introduced in the calculations. Numerical values of the pair density are found to be in the $1-2 \times 10^{12}$ cm^{-2} range. If we only take into account the nonperturbed Kleinman potential (6), we find that the experimental densities are outside the liquid domain and have larger values than the calculated liquid equilibrium density, which has no physical significance. The comparison between experience and calculus shows that the spectra recorded for the 4–13 nm QW's are well explained by carrier recombination in a 2D EHL.

In view of the simplicity of the model, more accurate calculations must be carried out and compared to our data. In particular, great care must be given to the form of the screened Coulomb potential in varying-thickness QW's with low l_z. The influence of image charges on this potential is also of importance. That is why a complete calculation of the kinetic and exchange-correlation energies with image charges at the Si/SiO_2 interfaces must be attempted from first principles using a nonscreened Coulomb interaction between carriers.

The band degeneracy set to 2 for the electrons and 1 for the holes is another important problem which has to be pointed out and deserves a more sophisticated treatment. The previous degeneracies are only available in the case of very small thickness, due to the complete splitting of the different energy bands of electrons and holes. In the frame of the effective mass theory and taking the case of electrons, one can give a crude estimate of the energetic splitting ΔE_Q between the two groups of electron valleys. Assuming a size reduction of the QW in the (100) direction, the first group is twofold degenerate with a mass $m_z = m_{el} \approx 0.92$ (Ref. 4) for motion perpendicular to the QW surface, whereas the second group is fourfold degenerate with $m_z = m_{et} \approx 0.19$ (Ref. 4). We take

$$\Delta E_Q = \frac{\hbar^2}{2}\left(\frac{\pi}{l_z}\right)^2\left[\frac{1}{m_{et}} - \frac{1}{m_{el}}\right]. \qquad (18)$$

The splitting is complete when the inequality $\Delta E_Q \geqslant E_F^e(n^{2D}) = \pi\hbar^2 n^{2D}/m_{et}g$ is fulfilled and gives the associated critical thickness l_z^c (E_F^e being the 2D Fermi quasilevel as given in Ref. 21). Assuming the density varies continuously between thick and narrow QW's, we can reasonably set $n^{2D}/l_z^c = n_0^{3D} \approx 3.2 \times 10^{18}$ cm^{-3}, and we find $l_z^c = 9.2$ nm. In the intermediate regime, when the band splitting is not yet achieved, several types of recombination are expected: of "hot" type, between the more split valence and conduction bands, of "cold" type, between the less split valence and conduction bands, and also recombination between "hot" and "cold" carriers. The recombination between carriers originating from these two groups of bands would result in a camel's-back-type spectrum in the intermediate thickness regime.

On the other hand, experiments as a function of $\mathcal{P}$ in narrow QW's are necessary to observe the two-dimensional free exciton at very low pumping powers and could be a very efficient way to measure the exciton work function. In such a case, these experiments could lead to check the accuracy of both the exciton and liquid binding energies.

B. Effects of variable injected carrier density in narrow quantum wells

As we did above for the 3D case in the first section, we use the usual variable-$\mathcal{P}$ method to determine the nature of the condensed phase in thin QW's. We can see in Fig. 8(a) PL spectra acquired under cw operation on the 4.7-nm QW at fixed temperature (T=6 K) and variable $\mathcal{P}$. As shown in Fig. 8(b), the line full width at half maximum (FWHM) is independent of pumping level, neglecting any broadening due to the weak contribution at 1.131 eV. This line is ascribed to the TA replica of bound on boron excitons (BE's) in the underlying bulk c-Si and negligibly alters the high-energy side of the QW PL spectra at low $\mathcal{P}$.

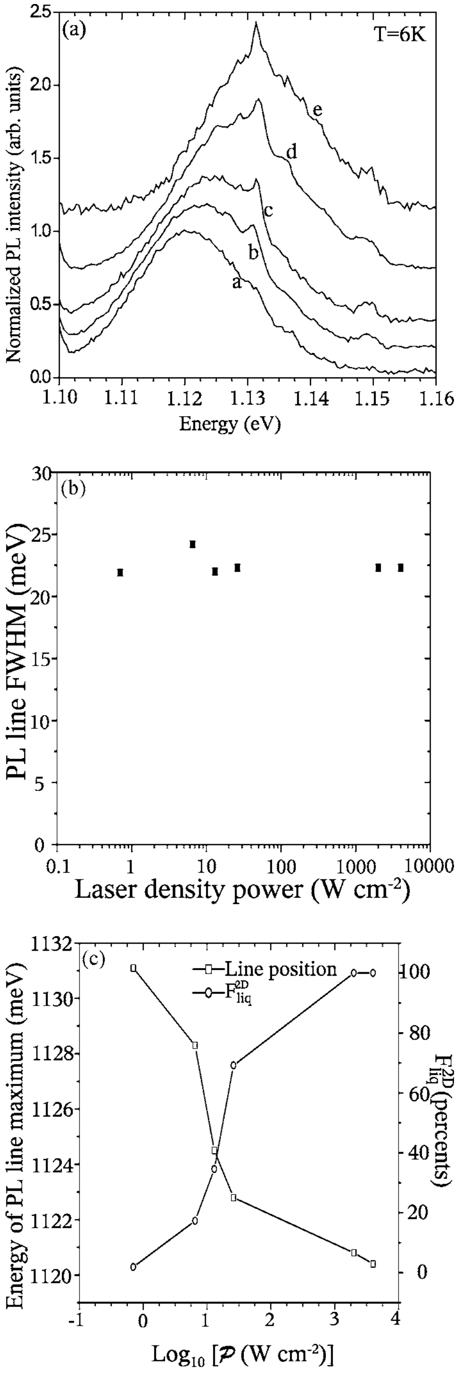

FIG. 8. (a) PL spectra acquired on a 4.7-nm QW at 6 K as a function of laser power with $\mathcal{P}=4\times10^3$ W cm^{-2} (curve a), 26 W cm^{-2} (curve b), 13 W cm^{-2} (curve c), 6.5 W cm^{-2} (curve d), and 0.7 W cm^{-2} (curve c). (b) Full width at half maximum of the recombination lines shown in (a). (c) Filling factor and line position as a function of $\mathcal{P}$ for the 4.7-nm QW.

This result differs from the 3D case where the change in the spectral shape associated with the Mott transition between the excitons and EHP is much more spectacular. Indeed, if we look at the 100-nm QW spectra reported in Fig. 1 and acquired above T_c, we can see that the plasma linewidth measured during the Mott transition reduces in a ratio of 1–2 corresponding to the low-density exciton state.

In view of the results reported in Fig. 8(c), and considering that the condensate linewidth only depends on the phase density at fixed temperature, we deduce that the intrinsic density of the photocreated e-h phase is constant in the 4.7-nm QW although the mean carrier density varies with $\mathcal{P}$. This clearly demonstrates that the e-h pairs condense into a constant-density liquid state, while the mean carrier density changes with the laser power. This comparison highlights the differences between the thick and thin QW's and shows the incompressible nature of the e-h fluid created in thin QW's under the above-mentioned physical conditions.

In contrast with the theory of electron hole liquids in bulk materials, spectra recorded in Fig. 8(a) slightly blueshift as $\mathcal{P}$ decreases, which is *a priori* surprising since keeping constant the density does not modify the band-gap renormalization energy ΔE_{BGR}. Here, we shall present a simple model in which the 2D EHL droplet coalescence plays an important role in the spectral properties. This 2D model is in complete analogy with the 3D model as discussed in Ref. 8 for the case of the 3D nanodroplets and uses the more "classical" surface energy picture[31] to give account of the spectral blueshift.

The QW thickness being of the order of magnitude of the bulk Bohr radius ($a_x^{3D}=4.9$ nm), the 3D EHL droplets cloud will undergo a change in the spatial carrier distribution in 2D systems towards a flat cloud of EHL pancakes with radius r_{xy}. The energy E_{xy} of a EHL pancake of radius r_{xy} containing N e-h pairs is written

$$E_{xy} = NE'_G + 2\pi r_{xy}\sigma_i + 2\pi r_{xy}^2\sigma_l, \tag{19}$$

where $E'_G(N/S)=E_g+E_G(N/S)-\hbar\omega_{TO}$ is the spectroscopic 2D liquid ground-state energy depending on the e-h pair density N/S, σ_i is the liquid surface energy per unit surface on the $\mathrm{Si/SiO_2}$ interface, and σ_l is the line energy per unit length on the pancake perimeter. Deriving Eq. (19) with respect to N gives us the pair chemical potential. When evaluated at the equilibrium density $n_0^{2D}=N/\pi r_{xy}^2$, we have

$$\mu(r_{xy}) = \mu(\infty) + \frac{2\sigma_i}{n_0^{2D}} + \frac{\sigma_l}{n_0^{2D} r_{xy}}, \tag{20}$$

where $\mu(\infty)$ denotes the high-energy PL cutoff of infinite-radius pancakes. The two other line and surface terms in Eq. (20) all positively contribute to the total pancake energy and are responsible of the line blueshift in finite-radius pancakes spectra. However, one can see that the surface contribution in the e-h pair chemical potential does not depend on the pancake size, which is not surprising since in the case of a 2D geometry the internal pancake energy NE'_G and the surface energy $2\sigma_i S$ vary in the same way as r_{xy}^2. In the framework of this model, the experimental shift of the 2D EHL PL lines under variable $\mathcal{P}$ is interpreted as a r_{xy}-dependent EHL pancake chemical potential arising from a change in the pancake perimeter and in the line energy.

In the coalescence model, the pancakes radius depends on the filling of the QW in 2D EHL, which can be evaluated in the same fashion as the pair density in thicker QW's [cf. Eq. (2)]. The filling factor F_{liq}^{2D} is defined as the mean pair to liquid densities ratio and is written

$$F_{liq}^{2D}(\mathcal{P}) = \frac{\mathcal{P}(1-R)A(l_z)\tau^{EHL}}{n_0^{2D} h\nu}, \tag{21}$$

with $n_0^{2D}\approx 2\times 10^{12}\ \mathrm{cm^{-2}}$ and $\tau^{EHL}\approx 200$ ns in a 28-nm QW at 6 K. In Eq. (21), we have neglected any carrier diffusion along the QW which would cause a slight deviation of F_{liq} towards lower values. This assumption agrees well with the formation of a condensed state of carriers under a liquid form. The filling factor and the line positions are reported in Fig. 8(c) as a function of $\mathcal{P}$. Two high- and low-$\mathcal{P}$ regimes emerge from the curve shapes, with an intermediate regime showing opposite variations of the two curves. This sets up a clear correlation between the QW filling and the line position and supports our hypothesis on the coalescence. In particular, in the $1\times 10^3\ \mathrm{W\,cm^{-2}}$ power range, F_{liq}^{2D} and the line position reach a saturation value of 100% and 1.121 eV, respectively, which correspond to the complete coalescence of EHL pancakes into a macroscopic EHL state and to the subsequent disappearance of the excess line energy. Strictly speaking, Eq. (21) gives values greater than 100% in the high-$\mathcal{P}$ range—more precisely of the order of 200%—corresponding to the creation of a uniform EHL layer spreading outside the laser spot area, but we preferred limiting F_{liq}^{2D} to the [0, 1] interval to keep physical significance.

The line energy σ_l can be found by measuring the PL energetic shift ΔE on spectra corresponding to PL emission by coalesced liquid (high $\mathcal{P}$) and EHL pancakes with radius r_{xy} (low $\mathcal{P}$). According to Eq. (20), we find $\Delta E=\sigma_l/n_0^{2D}r_{xy}$, where the unknown radius r_{xy} needs to be determined using the 2D extension of the 3D nanodroplet model.[8]

Due to many-body interactions leading to the band-gap lowering, 2D EHL pancakes can be viewed as QW's with barrier heights relative to the outside given by the carrier work functions $\Phi_e=\Phi_h=\Phi/2$. Assuming a gradual 2D parabolic potential of the form $V_{e,h}(\rho_{xy})=\frac{1}{2}m_{e,h}\omega_{eh}^2\rho_{xy}^2$ for both electron and hole energy bands, with the condition $V_{e,h}(r_{xy})=\Phi_{e,h}=\Phi/2$, the ground-state energy of a single particle immersed in the pancake is the solution of the 2D harmonic oscillator $\delta E_{e,h}=(\hbar/r_{xy})\sqrt{2\Phi_{e,h}/m_{e,h}}$, with $m_e=m_h=0.19$. The e-h pair excess energy resulting from the quantum confinement in small pancakes is identified with the spectroscopic blueshift at low $\mathcal{P}$, which provides the necessary relation to estimate the pancake radius and finally the line energy. Data give us $\Delta E\approx 10.7$ meV and the related numerical values $r_{xy}\approx 13.4$ nm and $\sigma_l\approx 2.9\times 10^6\ \mathrm{eV\,m^{-1}}$, obtained with the relations $\Delta E=\delta E_e+\delta E_h$ and $\Delta E=\sigma_l/n_0^{2D}r_{xy}$, with $\Phi\approx 12.8$ meV, as given by numerical calulations for the 4.7-nm QW and $n_0^{2D}=2.0\times 10^{12}\ \mathrm{cm^{-2}}$.

This result is in quantitative agreement with the observed 3D nanodroplet radius in a 28-nm QW (Ref. 8) set to 14 nm and strongly suggests to us that the characteristic size of a small e-h aggregate continuously passes from a 3D to a 2D geometry without noticeable radius modification. On the other hand, experimental measurements of the surface energy in bulk c-Si (Ref. 32) yield $\sigma_s=1.3\times 10^{13}\ \mathrm{eV\,m^{-2}}$. This term, when extrapolated to its "unidimensional" value, gives an idea of the estimated line energy $\sigma_l^{est}\approx\sqrt{\sigma_s}=3.6\times 10^6\ \mathrm{eV\,m^{-1}}$, in qualitative agreement with its experimental value. These data support the previous EHL pancake model and the assumptions on the coalescence and the influence of the line energy on the recombination spectra.

The EHL pancake model provides the simple "universal" relation for any semiconductor between the line energy, the 2D exciton work function, and the zero-temperature equilibrium density by equating the theoretical spectral blueshifts given in the two previous approaches—i.e., the line energy and the parabolic potential methods:

$$\frac{\sigma_l}{n_0^{2D}} = \hbar\sqrt{\Phi}\left(\frac{1}{\sqrt{m_e}} + \frac{1}{\sqrt{m_h}}\right). \qquad (22)$$

Measurements of the pancake radius by means of diffusion experiments would be of great interest to confirm the EHL pancake formation, as Pokrovskii and Svistunova[33] did for bulk Ge. This method would give a more accurate value of the line energy by precisely knowing r_{xy} and should be completed by a laser-power-dependent study of recombination spectra to determine Φ. These experiments would be a test to verify the pancake model relevance by checking the validity of Eq. (22).

C. Phase diagrams of carriers in narrow QW's

Phase diagrams of carriers in QW's give very important information about e-h condensation properties such as the critical temperature or liquid-gas phase boundaries. Many methods of calculation have been reported in bulk semiconductors and give satisfactory results when compared to the data. The "universal" method of the corresponding states of Guggenheim[34] based on the similarities of the interparticle potential of various species or the noninteracting droplet fluctuations model of Reinecke and Ying[35] cannot be adapted to our case. Indeed, in view of the Kleinman's model, the interparticle potential depends on the thickness and may lead to some shape modifications with respect to the "Guggenheim" potential at low thickness. Moreover, the lack of theoretical estimates of the line energy of EHL pancakes make it difficult to adapt the model of Reinecke and Vashishta to the 2D case. A very convenient way to draw up the 2D phase diagram would be to put the two conditions of mechanical and chemical equilibrium between 2D free excitons and 2D EHL.[4] In this method, the e-h pair energy needs to be computed over a wide range of density for a given thickness, which is an obstacle in the determination of the phase diagram.

Here, we use a simple spin-1 lattice-gas model adapted from the 3D approach of Droz and Combescot.[36] In our model, the 2D plasma is represented by a 2D square lattice of cells with "spin" $S_i(+1,-1,0)$ if the ith cell is occupied by one electron, one hole, or is empty. The Hamiltonian of the two-dimensional e-h system becomes

$$H = \frac{1}{2}J(x)\sum_{\langle i,j\rangle} S_i S_j - \mu\sum_i S_i^2 + Ax\sum_i S_i^2, \qquad (23)$$

where $x=\mathcal{N}/\mathcal{N}_0$ is the density of occupied cells, with $\mathcal{N}_0 = 2n_0^{2D}$ the total carrier density at zero temperature, equal to the number of cells, and $\mathcal{N}=n_e^{2D}+n_h^{2D}$. $J(x)$ is the screened Coulomb potential between two cells, whereas the proportionality constant A enters in the density-dependent kinetic term in Eq. (23). The Coulomb interaction between one cell and the other ones is limited to the four nearest-neighboring cells. In the mean-field approximation, one obtains the set of equations

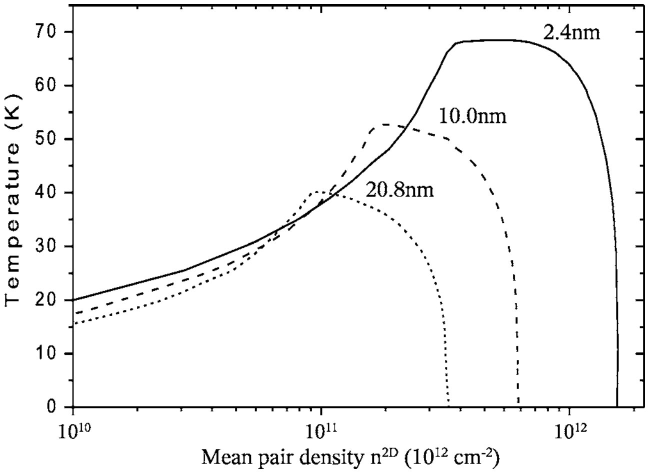

FIG. 9. Phase diagrams of carriers calculated with the spin-1 lattice-gas model for various QW thicknesses. The image charge effect has been neglected.

$$\mu(m,x,T) = Ax - k_BT\ln\frac{2(1-x)}{x} - k_BT\ln\left[\cosh\frac{4mJ(x)}{k_BT}\right], \qquad (24)$$

$$m = x\tanh(4J(x)m/k_BT) \quad (0 < m \leqslant 1), \qquad (25)$$

for the chemical potential and the spin thermal average at the ith cell.

$J(x)$ and A can be estimated by comparing the Hamiltonian given in Eq. (23) to the exchange-correlation and kinetic energies at zero temperature and $n=n_0^{2D}$, respectively. For $x=1$, we deduce $J(1)=|F_{xc}(n_0^{2D})|/8$ and $A=[E_F^e(n_0^{2D}) + E_F^h(n_0^{2D})]/4$. The density dependence of the Coulomb term is assumed to follow a "Kleinman" exponential law—i.e.,

$$J(x) \approx \frac{|F_{xc}(n_0^{2D})|}{8}\left(1 - \exp\left[-\frac{\gamma(l_z)}{a_x^{2D}\sqrt{\pi n_0^{2D}x}}\right]\right), \qquad (26)$$

γ being expressed in a_x^{2D} units. The exchange-correlation term F_{xc} and the quasi-Fermi levels at the equilibrium density n_0^{2D} are found after numerical calculations of the ground-state parameters as described in the previous section, with or without the influence of image charges. The phase diagrams are numerically computed thanks to Eqs. (24) and (25) using Maxwell construction. Here, only two parameters are necessary to construct the phase diagram of carriers for a given thickness—namely, n_0^{2D} and $F_{xc}(n_0^{2D})$—knowledge of which as a function of l_z makes possible systematic studies as a function of the thickness.

Results of calculations are reported in Fig. 9 for l_z=2.4, 10.0, and 20.8 nm. Here, image charges are not included in the calculus of the γ function. Each curve separates the free-exciton and liquid domains at low and high densities, respectively. The critical temperature is given by the highest point on each diagram and terminates the phase separation between a gas of excitons in equilibrium with a liquid and a compressible plasma as T is raised.

Lowering the thickness clearly modifies the shape of the phase diagrams: the critical temperature nearly doubles between 20.8 and 2.4 nm and reaches 69 K, well above its bulk value of 28 K, and the zero-temperature equilibrium density increases. This behavior originates from the rise in the 2D EHL binding energy at low thickness as deduced from previous calculations, resulting in a more vigorous increase in the exchange-correlation term $J(1)$ than in the kinetic term A as l_z is lowered. Thus, at low thickness, the extra kinetic energy due to the strong carrier localization is balanced by a more efficient stabilizing exchange-correlation energy, making the liquid stable up to elevated temperatures. This result is in the spirit of the universal relation observed in many bulk semiconductors between the liquid ground-state energy $|E_G|$ and the critical temperature T_c (Ref. 37)—i.e., $k_BT_c/|E_G| \approx 10\%$. Concerning narrow QW's, numerical estimates give constant values around 13%, which is very close to the bulk term and seems to indicate that the "bulk" relation is also valid in two dimensions.

Another important point related to the shape of the diagrams has to be addressed. The low-density sides of the diagrams in Fig. 9 show that at low temperature—i.e., out of the critical region—the exciton condensation density increases with l_z at constant temperature. This result is the signature in the diagram of the rise of the exciton work function when l_z decreases, as calculated in the previous section. The present phase diagram calculus is a supplementary indication that the 2D FE line is expected to vanish in very narrow c-Si QW's.

Although the spin-1 lattice-gas model is very simple, it brought very satisfactory results when applied to the case of bulk Ge (Ref. 36) and provided reevaluated theoretical phase diagrams in remarkable agreement with the experience after fitting of A and $J(1)$. However, in view of the sensitivity of the model to the A and $J(1)$ variations and of the uncertainty of the liquid ground-state parameter calculations, previous results concerning the phase diagrams should merely be interpreted qualitatively. Experimental determination of the phase diagram of a 2D e-h system would be of great interest, as the study of the influence of the thickness on the T_c variations, for instance.

V. CONCLUSION

Silicon QW's offer the unique opportunity to reinvestigate e-h condensation processes in confined media. Evidence has been reported for the formation of the exciton and electron-hole liquid-plasma phases in SOI QW's over a wide range of thickness, from 190 nm down to 4.7 nm. Several regimes have been identified, according to the range of thickness.

For the thickest wells ($l_z \geqslant 15$ nm), observation of steady-state and dynamical effects shows the crucial influence of the structural SiO_2 barriers on e-h condensation properties.

In the weak quantum confinement regime ($l_z \leqslant 15$ nm), evidence of the formation of an e-h condensed phase—a liquid and incompressible phase—under quantum confinement in c-Si QW's is made. In view of the simplicity of the model used here to analyze the data, some complementary calculations should be carried out to accurately compute the ground state of the two-dimensional EHL. In particular, great care should be taken by including the influence of image charges in the model. Comparison between experimental data and a more sophisticated theory could give very precious information on the magnitude of the contribution of these charges in the potential of carriers in the QW. We would like to point out that the experimental measurement of the phase diagrams of carriers in varying-l_z QW's is of importance since comparison between results of the many-body theories and data—equilibrium density and critical temperature—is straightforward. This later point requires extensive work but is necessary for further investigations of the two-dimensional electron-hole liquid.

---

*Present address: Université de Sherbrooke, département de génie électrique et génie informatique, 2500 boulevard de l'université, J1K 2R1, Sherbrooke, Québec, Canada. Electronic address: nicolas.pauc@usherbrooke.ca

†Electronic address: calvo@drfmc.ceng.cea.fr

[1] J. R. Haynes, Phys. Rev. Lett. **17**, 860 (1966).

[2] L. Keldysh, in *Proceedings of the 9th International Conference on the Physics of Semiconductors, Moscow, 1968*, edited by S. M. Rivkin and Yu. V. Shmartser (Nauka, Moscow, 1968), p. 1307.

[3] V. M. Asnin and A. A. Rogachev, JETP Lett. **7**, 360 (1968).

[4] T. M. Rice, J. C. Hensel, T. G. Phillips, and G. A. Thomas, in *Solid State Physics*, edited by H. Ehrenreich, F. Seitz, and D. Turnbull (Academic Press, New York, 1977), Vol. 32.

[5] M. Bruel, Nucl. Instrum. Methods Phys. Res. B **108**, 313 (1996).

[6] B. M. Bruel and A. J. Auberton-Herv, Jpn. J. Appl. Phys., Part 1 **36**, 1636 (1997).

[7] M. Tajima and S. Ibuka, J. Appl. Phys. **84**, 2224 (1998).

[8] N. Pauc, V. Calvo, J. Eymery, F. Fournel, and N. Magnea, Phys. Rev. Lett. **92**, 236802 (2004).

[9] S. Nihonyanagi and Y. Kanemitsu, Appl. Phys. Lett. **85**, 5721 (2004).

[10] D. E. Aspnes, in *Properties of Crystalline Silicon*, edited by R. Hull (Inspec, London, 1999).

[11] T. M. Rice, Nuovo Cimento Soc. Ital. Fis., B **23**, 226 (1974).

[12] P. Vashishta and R. K. Kalia, Phys. Rev. B **25**, 6492 (1982).

[13] R. B. Hammond, T. C. McGill, and J. W. Mayer, Phys. Rev. B **13**, 3566 (1976).

[14] *Handbook of Mathematical Functions*, edited by M. Abramowitz and I. A. Stegun (Dover, New York, 1964).

[15] M. Combescot, Phys. Rev. Lett. **32**, 15 (1974).

[16] A. F. Dite, V. D. Kulakovskii, and V. B. Timofeev, Sov. Phys. JETP **45**, 604 (1977).

[17] J. Shah, M. Combescot, and A. H. Dayem, Phys. Rev. Lett. **38**,

1497 (1977).

[18] L. M. Smith and J. P. Wolfe, Phys. Rev. B **51**, 7521 (1995).

[19] I. Balslev, Phys. Status Solidi B **101**, 749 (1980).

[20] J. Weber, in *Properties of Crystalline Silicon*, edited by R. Hull (Inspec, London, 1999).

[21] D. A. Kleinman, Phys. Rev. B **33**, 2540 (1986).

[22] A. T. Ando and F. Stern, Rev. Mod. Phys. **54**, 437 (1982).

[23] D. A. Kleinman, Phys. Rev. B **28**, 871 (1983).

[24] L. V. Keldysh, JETP Lett. **29**, 658 (1979).

[25] L. Keldysh, Phys. Status Solidi A **164**, 3 (1997).

[26] The $\gamma(l_z)$ function taking account of the image charge effect has been calculated using Eq. (9), assuming a total validity of $B_{EX}(l_z)$ in the whole range of thickness of Fig. 6(a).

[27] H. Kageshima, Surf. Sci. **357-358**, 312 (1996).

[28] S. B. Zhang and A. Zunger, Appl. Phys. Lett. **63**, 1399 (1993).

[29] Y. M. Niquet, C. Delerue, G. Allan, and M. Lannoo, Phys. Rev. B **62**, 5109 (2000).

[30] Strictly speaking, this condition for the minimization of $E(n^{2D},T)$ should be replaced by the two simultaneous conditions on the chemical potential μ—i.e., $\partial\mu(n^{2D},T)/\partial n^{2D} = \partial^2\mu(n^{2D},T)/\partial n^{2D\,2}=0$, with $\mu(n^{2D},T)=\partial n^{2D}E(n^{2D},T)/\partial n^{2D}$. The T term in Eq. (17) leads to a zero contribution in the μ derivatives and should be developed at higher orders to give account for any influence of the temperature on the μ derivatives. However, in view of the similar values obtained for T_c in the bulk c-Si by using the two methods (Ref. 4), we shall consider that our approximation is valid and gives satisfactory numerical values.

[31] B. Etienne, C. Benot la Guillaume, and M. Voos, Phys. Rev. Lett. **35**, 536 (1975).

[32] P. Voisin, B. Etienne, and M. Voos, Phys. Rev. Lett. **42**, 526 (1979).

[33] Ya. E. Pokrovskii and K. I. Svistunova, JETP Lett. **13**, 212 (1971).

[34] E. A. Guggenheim, J. Chem. Phys. **13**, 253 (1945).

[35] T. L. Reinecke and S. C. Ying, Phys. Rev. Lett. **35**, 311 (1975).

[36] M. Droz and M. Combescot, Phys. Lett. **51A**, 473 (1975).

[37] T. L. Reinecke and S. C. Ying, Phys. Rev. Lett. **43**, 1054 (1979).